Advanced Study of Switchable Spin Crossover Compounds

Gavin Craig

ADVANCED STUDY OF SWITCHABLE SPIN CROSSOVER COMPOUNDS

Universitat de Barcelona

Facultat de Química

Departament de Química Inorgànica

Programa de Doctorat: Química Inorgànica Molecular

Grup de Magnetisme i Molècules Funcionals

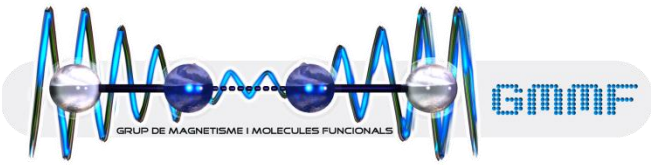

Gavin Craig

Director: Dr. Guillem Aromí Bedmar, Departament de Química Inorgànica

Tutor: Dr. Santiago Alvarez Reverter, Departament de Química Inorgànica

Contents

Chapter 9: Magneto-structural correlations

9.0 Introduction

On one level, the interplay between packing forces and the shape of the ligands and resulting cations helps determine the local geometry around the metal centre of the SCO systems discussed in previous Chapters. The distortion of cations in the quintet state has previously been studied for the systems containing 1-bpp,[1, 2] and the class of compounds with the general formula $[FeL_n(NCS)_2]$,[3] where L_n = a variety of nitrogen donor ligands. The degree of distortion in these compounds was evaluated using a series of parameters – θ, Φ, Σ, Θ – that focus on the cations within the systems, rather than the long range packing as effected by intermolecular interactions. The trend outlined in these studies was that the LS species lie closer to a regular octahedron for a given system than its HS counterpart. This conclusion was also reached by a study using continuous symmetry measures (CSMs).[4] That study looked at the correlation between two potential ideal symmetries for a hexa-coordinated metal centre, whether O_h or trigonal prism, and concluded that LS ions were closer to occupying ideal octahedra than were HS ions.[5]

On a longer range, Hirshfeld surface analysis[6] is starting to be used in SCO research.[7, 8] This type of study affords an unbiased description of the intermolecular interactions and crystal packing within a system. As such, it depends less on the importance apportioned to a given contact between lattice entities, and provides a description of the intermolecular interactions based on the electron density of the crystal contents. The conversion of the surfaces into 2D fingerprint plots[9] gives an unequivocal method of demonstrating the degree to which two or more crystal structures are similar or not.

The in-depth study of the packing forces undertaken in the preceding Chapters focussed on an overall view of how the lattice entities in the compounds that have been synthesised in this thesis order over the long range. Observations were made on how subtle changes in the action of lattice components, both spin-active and spin-inactive, could modify the supramolecular contacts between the cations, anions, and solvent molecules in the crystal structure. Here, the effect that these packing forces bring to bear on the cation and its shape and level of distortion will be described. This begins by using the four distortion parameters mentioned above, applying them both to the compounds obtained in this thesis, and to the entire class of 3-bpp-containing mononuclear compounds found in the

literature. This analysis is also complemented by CSMs. The longer-range effects of the intermolecular interactions are then evaluated by Hirshfeld surface analysis.

9.1 Definition of the parameters employed

The first section of the analysis of structural distortion employs four parameters which were defined in Chapter 3 (Section 3.2) and have been used throughout the thesis: θ, Φ, Σ, Θ. Briefly, θ measures the dihedral angle formed by the least-squares planes of the two *mer*- coordinated ligands.[10, 11] The second parameter, Φ, corresponds to the trans N-Fe-N angle formed by the coordination of the central pyridyl rings to the Fe(II) ion.[11] Consequently, these parameters have ideal values of 90° and 180°, respectively. These parameters give an indication of how the ligands are oriented with respect to each other, which gives the anion its particular shape.[2]

The parameters Σ and Θ, on the other hand, measure a local distortion around the Fe(II) ion.[13, 14] The value of Σ corresponds to the sum of the deviation away from 90° of the twelve possible *cis*-N-Fe-N bite angles, following Equation 9.1.[15] With the value of Θ, one obtains a measure of the twist away from perfect octahedral symmetry, O_h, towards a trigonal prismatic symmetry, D_{3h}. This analysis is based on the superposition of the opposite triangular faces of an octahedron, which ideally should present *cis*- angles of 60°. In D_{3h} symmetry, these angles are 0° because the triangles are superposed perfectly. There are 24 such N-Fe-N angles, and Θ is the sum of their deviation from 60° (Equation 9.2).[15]

$$\Sigma = \sum_{i=1}^{12} |90 - \alpha_i| \quad (9.1)$$

$$\Theta = \sum_{j=1}^{24} |60 - \beta_j| \quad (9.2)$$

Previous analyses have demonstrated that complexes in the HS state are associated with greater flexibility, allowing them to reach higher degrees of distortion than LS systems. In fact, in one set of systems, extreme distortion of the HS state was suggested to trap the compound in a HS state, causing a barrier to its possible transition to the singlet state.[11] Such a study had not been carried out on systems with the ligand 3-bpp, or its derivatives, and in the next Section, a discussion of the compounds obtained in this thesis will be held.

Compound	REFCODE	Cation Spin (Temp/K)	θ/°	Φ/°	Σ/°	Θ/°
i	HECCOJ	Mixed(90)	89.19	173.13	121.56	399.17
i	HECCOJ01	HS(250)	88.10	171.78	146.42	482.09
1	ITINOP	HS(200)	74.94	177.01	145.85	469.18
1	ITINOP01	HS(150)	74.90	177.12	144.72	466.03
1	ITINOP02	LS(100)	77.17	178.53	100.52	311.17
1	ITINOP03	LS(150)	77.54	178.62	100.13	310.82
1	ITINOP04	HS(100)	74.66	177.05	144.26	464.04
1	-	HS(30)	73.99	176.40	147.26	471.89
2	-	HS(150)	84.53	174.78	148.54	471.35
3	-	HS(100)	74.75	176.96	146.27	460.83
4	HECCID	HS(100)	73.34	151.36	171.12	501.97
5	HECCEZ	HS(100)	79.57	146.71	184.92	523.91
6	HECBUO	HS(150)	78.03	175.60	152.63	492.75
7	-	HS(250)	77.25	177.09	142.65	467.17
7	-	Mixed(90)	75.07	176.76	142.45	460.18
8	HECCAV	HS(100)	77.34	174.88	142.20	466.44
9	-	HS(100)	74.06	178.18	141.23	451.69
11	-	HS(100)	89.86	153.47	158.79	492.23
12	-	HS(100)	76.64	154.04	167.44	507.06
13	-	HS(100)	79.35	153.33	169.35	491.20
14	-	HS(100)	86.05	155.53	161.77	499.81

Table 9.1: Distortion measurements for all of the mononuclear Fe(II) complexes presented in this thesis.

9.2 Compounds obtained in this thesis

A compilation of the parameters defined in Section 9.1 is given in Table 9.1 for the mononuclear Fe(II) compounds obtained during the course of this thesis. The compounds synthesised using the novel polypyrazolyl ligands can display values of θ that are significantly below 90°, especially when compared with compound **i**, which is the only system to contain solely 3-bpp as the chelating species. This is a direct consequence of the functionalisation of the 3-bpp core. Because the central pyrazolyl rings are bound to the Fe(II) centre, they have little range of movement. However, in the wings of the

ligands H_4L and H_2L1, the unbound aromatic rings are more free to rotate around the bond to the pyrazolyl ring, moving in and out of the plane, with additional freedom provided by the hydroxy- or methoxy- groups, which twist to participate in hydrogen bonding motifs. The packing forces exerted therefore by the other lattice components have a greater effect on systems with the polypyrazolyl ligands. This effect is also observed in the parameter Φ. In general, the compounds lie in the range 170-180°, although the extreme nature of the packing induced in the compounds **4**, **5**, and those containing the ligand H_2L1, sees values of less than 160°. These compounds are also those which show the greatest level of deformation in terms of the parameters Σ and Θ. These parameters for the other compounds lie within a range of 140-150° for Σ in the HS state, moving towards values of 100° on undergoing SCO. Meanwhile, **4**, **5**, and the H_2L1 systems display values in excess of 165°. This tendency is also observed in Θ, although the difference with respect to the other compounds is not as pronounced.

9.3 Extension to the family of 3-bpp derivatives in the literature

This study was taken beyond the compounds obtained in this thesis, to the entire class of mononuclear Fe(II) systems containing 3-bpp derivatives as found in the literature. The calculated parameters for these compounds are given in Table 9.2. It is remarkable that so few systems show SCO on directly measuring the magnetic properties. The majority require the sample to be heated before any spin transition behaviour can be registered, usually after the consequent dehydration process. Figure 9.1 shows representations of the parameter Φ vs. θ and Φ vs. Σ. There is a notably lower distribution of values for the compounds that remain in the LS state, which are found closer to the ideal measurements of 180° and 90° in the cases of Φ and θ, respectively, and at generally lower values of Σ. While it appears that values of Φ below 170° inhibit a thermal SCO, the possibility of a transition is unrelated to the dihedral angle θ. The relationship between Φ and the bite angles around the Fe(II) centre result in compounds with low values of Φ having high values of Σ. It is also clear that on undergoing SCO, the dihedral angle comes closer to the ideal value.

A considerably more marked correlation is observed between Θ and Σ, analogous to a similar trend seen in systems containing 1-bpp (Figure 9.2).[1] In fact, this relationship is so clear that it allows characteristic ranges to be established for complexes in the HS, LS, and mixed states. In the HS state, the distortion around the Fe(II) centre is associated with

Formula	REFCODE	Cation Spin (Temp/K)	θ/°	Φ/°	Σ/°	Θ/°	Comment
$[Fe(3\text{-}bpp)_2]Cl_2 \cdot 6.5H_2O$	CAZJET[16]	LS(294)	89.64	178.9	96.17	315.45	Both the hydrate and the dehydrated sample are LS at RT. No SQUID data presented.
$[Fe(3\text{-}bpp)_2][MnCr(ox)_3]_2 \cdot (3\text{-}bpp) \cdot MeOH$	EDATOT[17]	Measurements suggest co-existence of HS and LS centres at all temperatures, but no clear evidence of SCO.					
$[Fe(3\text{-}bpp)_2][Cr(phen)(ox)_2]_2 \cdot 0.5H_2O$	GIVZAN[18]	LS(180)	88.62	176.5	90.75	298.41	Rehydrated form of GIVZER, SQUID shows a HS population of 28 %. SCO after dehydration.
$[Fe(3\text{-}bpp)_2][Cr(phen)(ox)_2]_2 \cdot 0.5H_2O \cdot 0.5MeOH$	GIVZER[18]	HS/LS(180)	86.41 /88.25	169.85/176.12	153.22/93.67	505.5 /308.02	50/50 mix of HS and LS cations. SCO after dehydration.
$[Fe(3\text{-}bpp)_2][Cr(phen)(ox)_2]_2 \cdot 5.5H_2O \cdot 2.5MeOH$	GIVZIV[18]	HS(180)	82.85	167.26	157.76	510.09	SQUID shows a residual LS population of ~10%. Dehydration gives a very, very gradual SCO.
$[Fe(3\text{-}bpp)_2]_2[Cr(ox)_3](ClO_4) \cdot 5H_2O$	ILACON[19]	LS/LS(294)	88.24 /88.91	176.36/179.31	94.55/89.60	294.48 /309.92	LS, with SCO induced by dehydration of the sample.
$[Fe(3\text{-}mbpp)_2](BF_4)_2 \cdot 2H_2O$	KALWUR[20]	HS/LS (150 K)	90/90	180/180	149.80/96.56	490.57 /316.84	After heating to 350 K, there is a hysteresis loop of 65 K.
$[Fe(3\text{-}mbpp)_2](BF_4)_2$	KALXAY[20]	LS(150 K)	90	180	110.84	363.20	LS form of KALXAY01, however no bulk magnetism could be measured.

Table 9.2: Distortion parameters for the mononuclear Iron compounds containing 3-bpp derivatives in the CSD. Abbreviations: ox = oxalate, phen = 1,10-phenanthroline, bpy = 2,2'-bipyridine, bpmdc = N,N'-bis(4-pyridyl-methyl)diaza-18-crown-6, 3-mbpp = 2,6-bis[5-methyl-1H-pyrazol-3-yl]pyridine.

Formula	REFCODE	Cation Spin (Temp/K)	θ/°	Φ/°	Σ/°	Θ/°	Comment
$[Fe(3\text{-}mbpp)_2](BF_4)_2$	KALXAY01[20]	HS(300 K)	90	180	141.68	464.43	See comment for KALXAY.
$[Fe(3\text{-}bpp)_2][Cr(bpy)(ox)_2]\cdot 2H_2O$	LAQYIM[21]	HS/LS (180)	83.84 /86.60	170.14/175.31	170.81/92.19	497.29 /303.47	50/50 HS/LS which turns fully HS on dehydration, and then displays SCO.
$[Fe(3\text{-}bpp)_2][Cr(bpy)(ox)_2]\cdot 2H_2O$	LAQYIM01[21]	HS(180)	84.56	173	149.17	490.51	Rehydrated form of LAQYIM that is fully HS. Undergoes SCO on dehydration.
$[Fe(3\text{-}bpp)_2](SCN)_2\cdot 2H_2O$	NEMSAZ[22]	HS(294)	89.52	175.16	146.99	482.63	Recrystallised sample from a bulk. The crystals show a less abrupt SCO than the bulk, with hints of a hysteresis loop.
$[Fe(3\text{-}bpp)_2](SeCN)_2$	NEMSED[22]	HS(294)	89.92	177.68	147.17	487.72	Recrystallised sample from a bulk. Shows less abrupt SCO.
$[Fe(3\text{-}bpp)_2](SeCN)_2\cdot 0.25(CH_3NO_2)\cdot H_2O$	NEMSIH[22]	HS/LS/ LS/LS (294)	87.36/ 89.84/ 88.25/ 88.14	168.90/ 176.78/ 177.44/ 178.91	145.31/ 100.44/ 96.90/ 92.64	479.14/ 328.05/ 318.12/ 303.04	No magnetic characterisation described.
$[Fe(3\text{-}bpp)_2](CF_3SO_3)_2\cdot 3H_2O$	NUPNIV[23]	LS(294)	86.77	177.11	94.19	309.36	LS at RT. Heating causes dehydration and the monohydrate shows SCO with a broad hysteresis loop.

Table 9.2 (cont.) Distortion parameters for the mononuclear Iron compounds containing 3-bpp derivatives in the CSD. Abbreviations: ox = oxalate, phen = 1,10-phenanthroline, bpy = 2,2'-bipyridine, bpmdc = N,N'-bis(4-pyridyl-methyl)diaza-18-crown-6, 3-mbpp = 2,6-bis[5-methyl-1H-pyrazol-3-yl]pyridine.

Formula	REFCODE	Cation Spin (Temp/K)	θ/°	Φ/°	Σ/°	Θ/°	Comment
$[Fe(3\text{-}bpp)_2](BF_4)_2 \cdot 3(C_4H_{10}O)$	OCUVAL[24]	Mixed(150)	87.83	174.37	131.27	431.07	Mixed HS/LS, however SCO demonstrated in solution in a variety of solvents.
$[Fe(3\text{-}bpp)_2](BF_4)_2 \cdot 2(CH_3NO_2)$	OCUVEP[24]	LS(150)	86.56	180	97.12	318.55	Crystal structure LS, however SCO demonstrated in solution in a variety of solvents.
$[Fe(3\text{-}bpp)_2](BF_4)_2 \cdot 2(CH_3NO_2) \cdot 2(C_6H_{14}O)$	OCUVIT[24]	LS(150)	88.13	177.46	95.23	312.72	Crystal structure LS, however SCO demonstrated in solution in a variety of solvents.
$[Fe(3\text{-}bpp)_2](BF_4)_2 \cdot 2(CH_3CN)$	OCUVOZ[24]	Mixed(150)	87.08	180	130.48	427.19	Mixed HS/LS, however SCO demonstrated in solution in a variety of solvents.
$[Fe(3\text{-}bpp)_2](C_9H_{10}O_6) \cdot 5.5H_2O$	OGIJEU[25]	HS(150)	87.55	167.15	143.76	474.21	HS, gives SCO after dehydration.
$[Fe(3\text{-}bpp)_2][Cu(Se_2C_4H_2N_2)_2] \cdot 3(CH_3CN)$	SOJKUY[26]	HS(180)	88.94	176.62	148.50	483.98	HS, no SCO.

Table 9.2 (cont.) Distortion parameters for the mononuclear Iron compounds containing 3-bpp derivatives in the CSD. Abbreviations: ox = oxalate, phen = 1,10-phenanthroline, bpy = 2,2'-bipyridine, bpmdc = N,N'-bis(4-pyridyl-methyl)diaza-18-crown-6, 3-mbpp = 2,6-bis[5-methyl-1H-pyrazol-3-yl]pyridine. Distortion parameters for the Iron compounds containing 3-bpp derivatives in the CSD.

Formula	REFCODE	Cation Spin (Temp/K)	θ/°	Φ/°	Σ/°	Θ/°	Comment
$[Fe(3\text{-}bpp)_2][Fe(CN)_5(NO)]$	UJEDOC[27]	LS(100)	81.49 /81.63	175.78 /179.96	102.41 /102.22	317.49	LS state of UJEDOC01, cooperative SCO with hysteresis loop of 3 K.
$[Fe(3\text{-}bpp)_2][Fe(CN)_5(NO)]$	UJEDOC01[27]	HS(294)	74.74	180.00	159.78	491.12	HS state of UJEDOC.
$[Fe(3\text{-}bpp)_2]I_2\cdot 4H_2O$	WEYVUR[28]	LS(294)	89.99	179.18	95.6	313.77	LS, however the dehydrate gives SCO with hysteresis.
$[Fe(3\text{-}bpp)_2](BF_4)_2\cdot 3H_2O$	WEYWAY[28]	LS(294)	87.35	179.26	94.43	309.99	LS, although the dehydrate gives SCO with hysteresis.
$[Fe(3\text{-}bpp)_2][Cr(bpy)(ox)_2](ClO_4)\cdot EtOH\cdot 4H_2O$	WUJCEK[29]	HS(180)	85.57	167.35	143.68	474.27	HS, SCO after dehydration.
$[Fe(3\text{-}bpp)_2][Cr(phen)(ox)_2](ClO_4)\cdot 1.5EtOH\cdot 4H_2O$	WUJCIO[29]	HS(180)	85.94	166.57	149.64	494.63	HS, SCO after dehydration.
$[Fe(3\text{-}bpp)_2][bpmdcK](SeCN)_{1.7}(ClO_4)_{1.3}\cdot MeOH\cdot H_2O$	YABKET[30]	LS(123)	90.00	178.13	91.76	301.25	LS, SCO after dehydration.
$[Fe(3\text{-}bpp)_2]_4[bpmdcH_2(H_2O)_2](ClO_4)_{10}\cdot 3MeOH\cdot 7H_2O$	YABKIX[30]	LS(123)	84.29	178.07	93.75	303.16	LS, SCO after dehydration.

Table 9.2 Distortion parameters for the mononuclear Iron compounds containing 3-bpp derivatives in the CSD. Abbreviations: ox = oxalate, phen = 1,10-phenanthroline, bpy = 2,2'-bipyridine, bpmdc = N,N'-bis(4-pyridyl-methyl)diaza-18-crown-6, 3-mbpp = 2,6-bis[5-methyl-1H-pyrazol-3-yl]pyridine

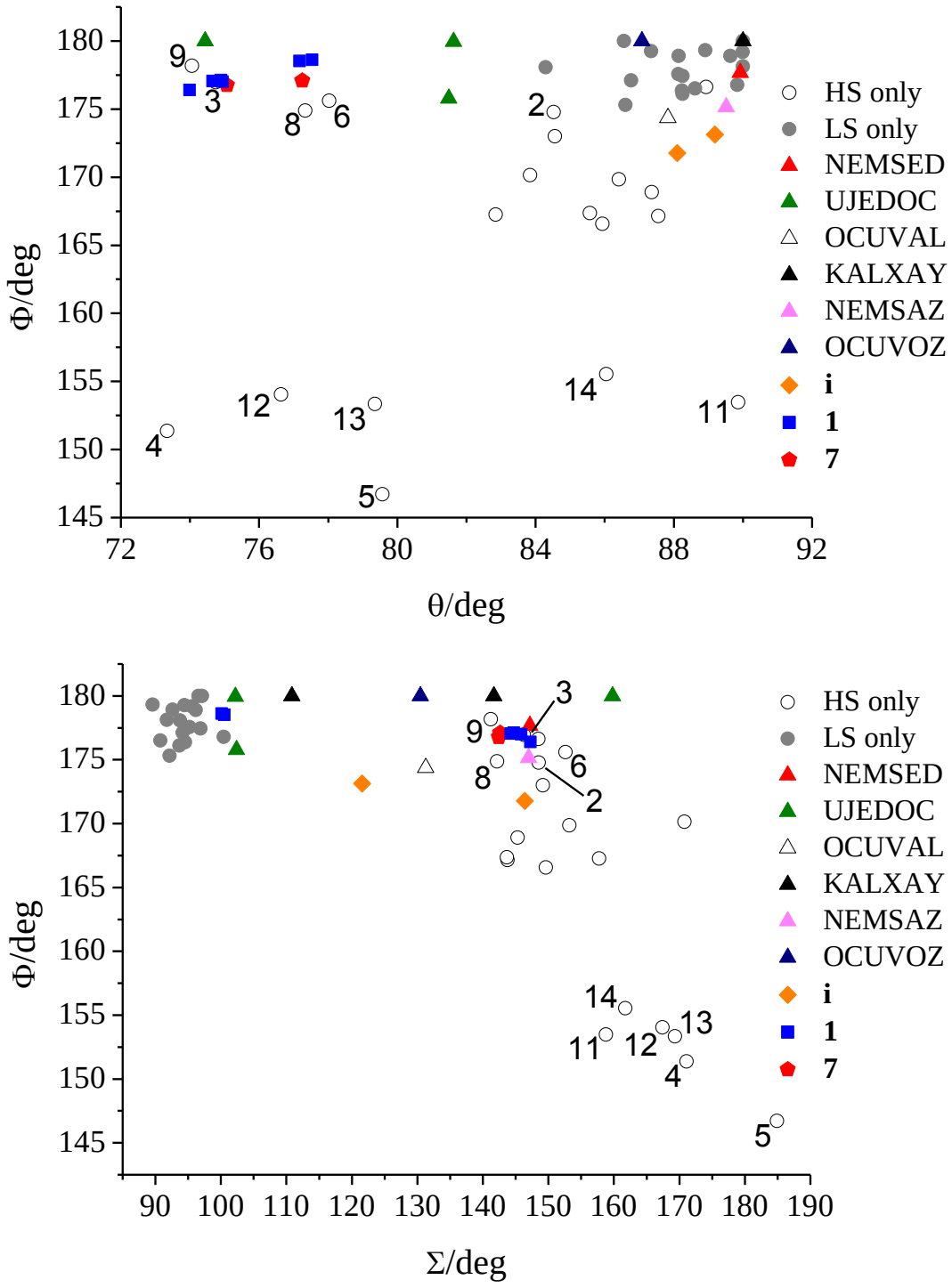

Figure 9.1: (top) Representation of Φ vs. θ and (bottom) of Φ vs. Σ for the structural data available from the CSD.

Σ > 140° and Θ > 450°, with the LS state at much lower values: Σ < 105° and Θ < 330°. Of the four points that lie between this range, three (**i**, OCUVAL,[24] and OCUVOZ[24]) have had SQUID measurements performed that confirm their mixed spin character. In the case of KALXAY,[20] the Fe(II) salt was found to be highly hygroscopic, such that a bulk

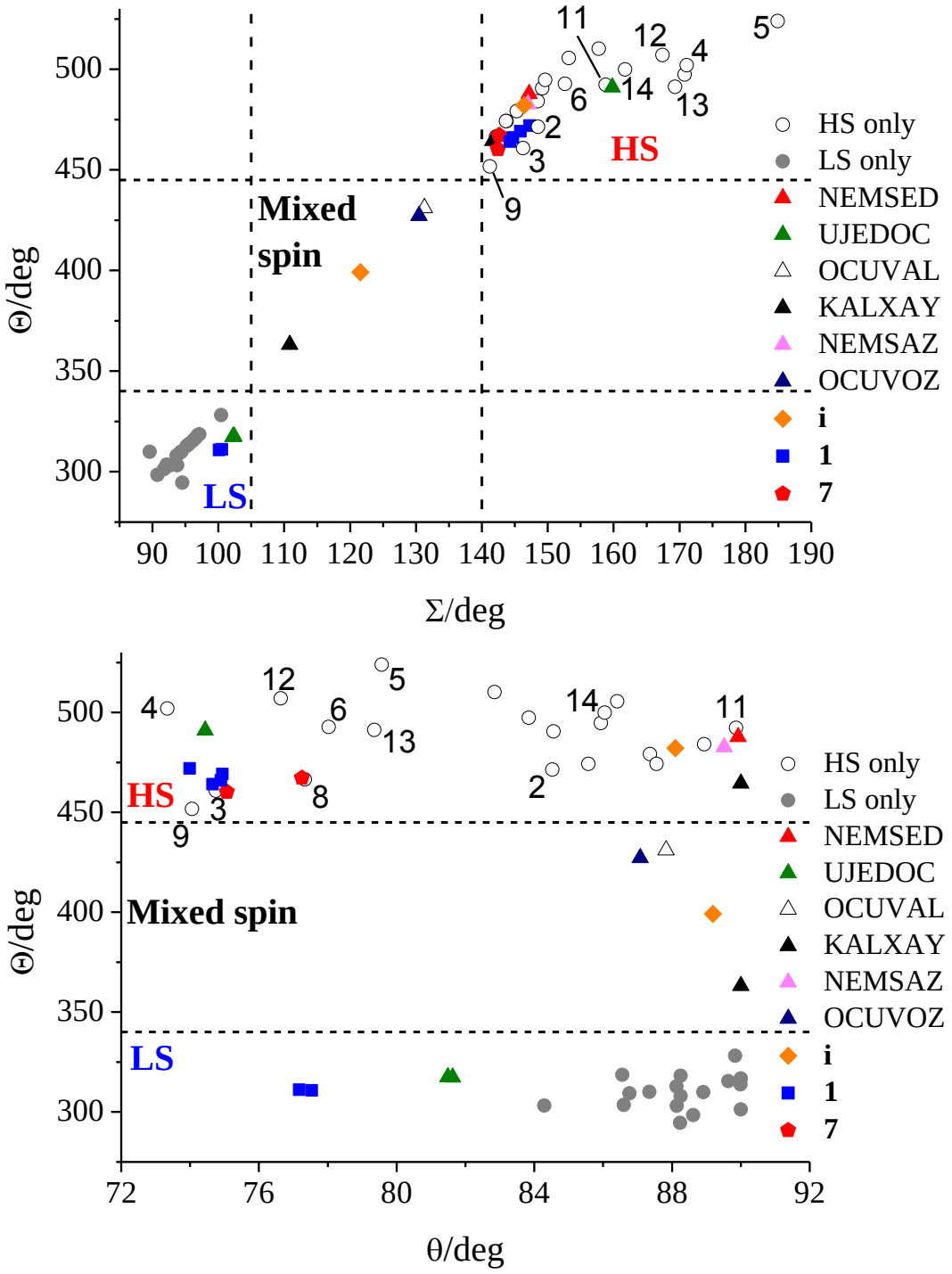

Figure 9.2: (top) Representation of Θ vs. Σ (Compound **8** is obscured) and (bottom) Θ vs. θ for the structural data available from the CSD.

magnetic measurement wasn't possible. Although the authors describe the system as undergoing SCO from HS to LS, the correlation presented in Figure 9.2 suggests that the transition is from a HS state to a mixed HS/LS state, with a majority LS population.

These correlations confirm the association of LS states with more ideal octahedral symmetries. It also includes the extreme distortions that have been previously observed in HS compounds. These deviations have been explained in the literature as consequences of Jahn-Teller distortion, whereby the degeneracy of the e_g orbitals is removed drastically through the twist of the Fe-N bonds away from the octahedron.[11] In the plot of Θ vs. θ (Figure 9.2), the tendency of the spin states to display certain values of the parameter Θ separates the compounds into two broad distributions over θ, with the mixed systems lying between these two bands. Again, θ is shown to have very little correlation with other structural parameters.

9.4 Continuous Symmetry Measures (CSMs)

In a previous work by Alvarez, Continuous Symmetry Measures were employed to study a wide range of parameters that are affected by a spin transition.[5] The study understood the structural changes observed in systems containing chelate ligands on the basis of a reduction in the normalised bite, *b*, occurring on SCO ($b = d/r$, where d is the donor···donor distance within a chelate ring, and r is the Fe-N bond length), which induces a transition away from the more octahedral geometry of the LS state towards a more trigonal prismatic geometry in the quintet state. Therefore, there exist two possible extremes of symmetry in these cases: an ideal octahedron (O_h), or an ideal trigonal prism (*itp*), with a pathway between the two which passes through intermediates of D_3 symmetry following the Bailar twist.[31] Therefore, to assess the symmetry in systems containing 3-bpp, the program SHAPE 2.0, partly developed in the Departament de Química Inorgànica of the Universitat de Barcelona, was used. The results are displayed in Figure 9.3, where $S(O_h)$ vs. $S(itp)$ is plotted, together with a solid line tracing the Bailar twist pathway. Here, a cation possesses an ideal symmetry if its value S for a given symmetry is zero. As could be anticipated from the previous discussion, HS systems have a more distorted coordination octahedron when compared to LS systems; *i.e.* they have higher values of $S(O_h)$. They also span a greater range of values in $S(O_h)$ than the LS cations. The LS systems have lower values of $S(O_h)$ and higher values of $S(itp)$ than the HS cations, which means that they present a more regular octahedron. The fact that the LS systems are not closer to ideal octahedral symmetry, and that both the HS and LS cations deviate substantially from the Bailar twist, is attributed to the geometrical

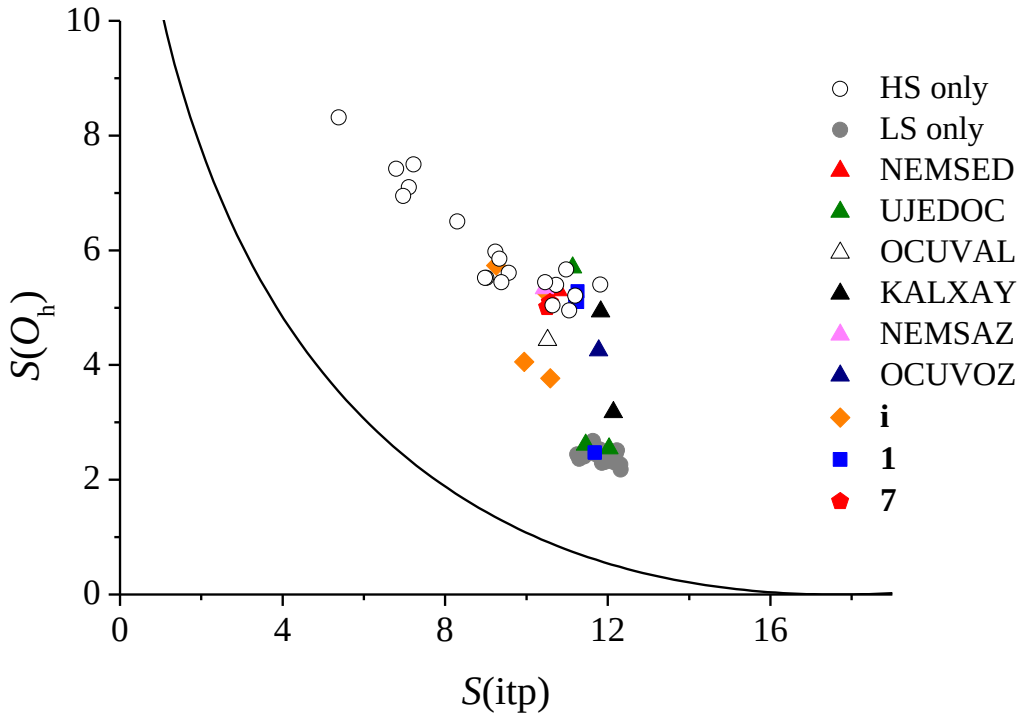

Figure 9.3: Plot of the octahedral and trigonal prismatic symmetry measures for all of the mononuclear Fe compounds containing the 3-bpp ligand and its derivatives. The solid line represents the Bailar twist pathway.

constraints imposed by the nature of the ligands, which doesn't allow for sufficient structural flexibility.

What remains unclear from these studies is whether the defining factor in the shape and symmetry displayed by a cation in these systems is determined by local factors (the bite angle, or Jahn-Teller distortions) or by the action of the packing in the crystal lattice. While previous Chapters have discussed this packing in a qualitative fashion, based on the observation of how certain interactions help assemble a lattice, the following section will use more quantitative methods to study the crystalline network.

9.5 Hirshfeld Surface analysis

As has been demonstrated in the preceding Chapters, the ligands developed in this thesis favour arrays of contacts between the various network components. Although this study involved the itemisation and measurement of hydrogen bonding motifs or other supramolecular interactions, recently the program CrystalExplorer 3.0[32] became freely available, which allows the calculation of the Hirshfeld surfaces associated with lattice entities, and from there, an appreciation may be gained of the overall nature of the

packing forces.[33] A Hirshfeld surface is a surface that surrounds that volume in space within which the electron density of the molecule of interest (the *promolecule*) predominates over the contribution of any other crystal component (the *procrystal*).[6] These surfaces then give a visual representation of the strength of the intermolecular contacts in which the promolecule participates via a colour scale. This scale has at its extremes red for the shortest contacts (*i.e.* the strongest interactions), and blue for the longest (weakest) passing through white. From this surface, a 2-dimensional "fingerprint" plot may be generated.[9] Each point on the surface can be characterised by a pair of indices, d_i and d_e, which correspond to the distances to nearest atom *inside* the surface and to the nearest atom *outside* the surface, respectively. The fingerprint is therefore the result of plotting the fraction of surface points for each of these possible (d_i, d_e) pairs.

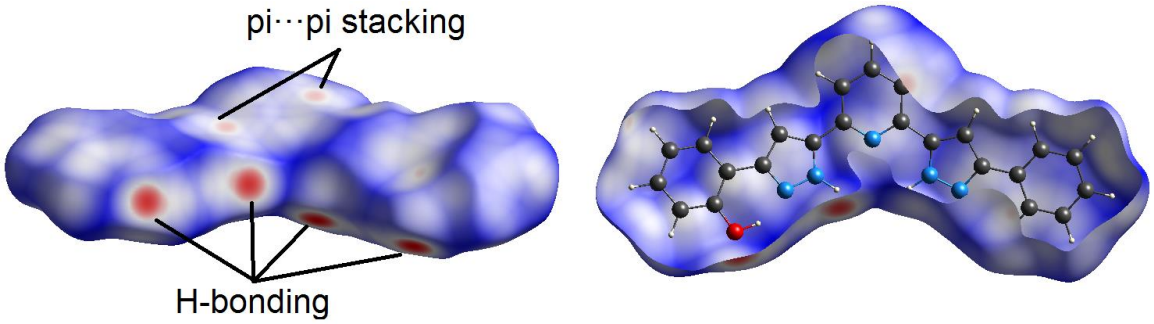

Figure 9.4: (left) Hirshfeld surface of the ligand H_4L, with a cut-away view of the surface and ligand (right).

This type of analysis is therefore interesting in SCO compounds, where often changes in the SCO behaviour are rationalised on the basis of the intermolecular interactions. However, the use of this technique in SCO research has so far been scarce.[7, 8] It could be applied to the complexes described in this thesis, where the cation usually doesn't vary over a series of compounds, and the variation in the lattice is largely due to anions and solvent molecules. To begin this study, the Hirshfeld surface and corresponding fingerprint plots were calculated for the ligand H_4L (Figures 9.4 and 9.5). On the surface, there are strong red patches around the heteroatoms which participate in hydrogen bonding interactions. These interactions consist of N-H as a hydrogen bonding donor, and the O atom of the O-H group as a hydrogen bond acceptor. The possibility of the O-H group as a hydrogen bonding donor is negated by the formation of an intramolecular hydrogen bond with the adjacent pyrazolyl ring. The faces of the ligand are mostly coloured blue and white, indicative of little interaction with other molecules in the lattice.

However there are two slightly red patches which correspond to $\pi\cdots\pi$ interactions. When converted to a fingerprint, these assignments are corroborated. There is a diagonal feature at (0.8, 1.2) and (1.2, 0.8) which correspond to the hydrogen bonding N-H···O donor, and the O···H-N acceptor, respectively. The highest number of contacts is displayed at (1.8, 1.8), equivalent to a distance of 3.6 Å, and significant of C···C contacts which form part of the $\pi\cdots\pi$ interactions.

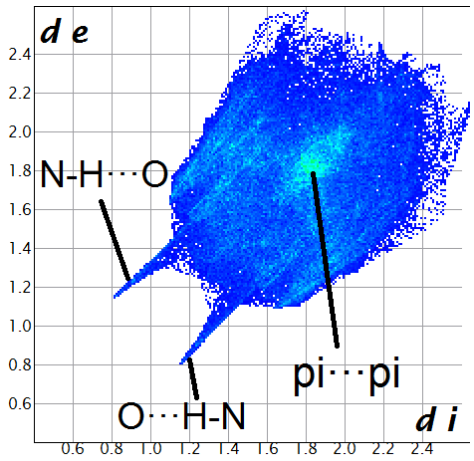

Figure 9.5: 2D fingerprint plot derived from the Hirshfeld surface of the ligand H_4L.

The next step was then to apply these techniques to the coordination compounds obtained during the thesis. The first thing to notice about the fingerprint plot that accompanies the study of compound **i** is that it is markedly asymmetric when compared to that of the H_4L ligand (Figure 9.7). This is due to the fact that it has been generated from a Hirshfeld surface of only one lattice component – the $[Fe(3\text{-bpp})_2]^{2+}$ cation – such that the (d_i, d_e) points that correspond to contacts with other lattice entities (solvents, anions) are not reciprocated by their (d_e, d_i) partner. This was not the case for H_4L, where the ligand is the only component in the crystal lattice, giving rise to the diagonal symmetry of the fingerprint. The surface generated for the cation of **i** (Figure 9.6) displays the hydrogen bonding motifs brought about by the interaction of the pyrazolyl rings with the anions and solvent molecules in the lattice that were described in Chapter 3. Except those interactions, and a slight indication of H···H contacts, the surface is largely featureless. This is consistent with the previous analysis, which could find no $\pi\cdots\pi$ contacts within the crystal lattice. This is further illustrated in the fingerprint, where there is no appreciable accumulation of peaks at (1.8, 1.8). The head-on H···H contacts are present in the form of the diagonal spike indicated in the Figure.

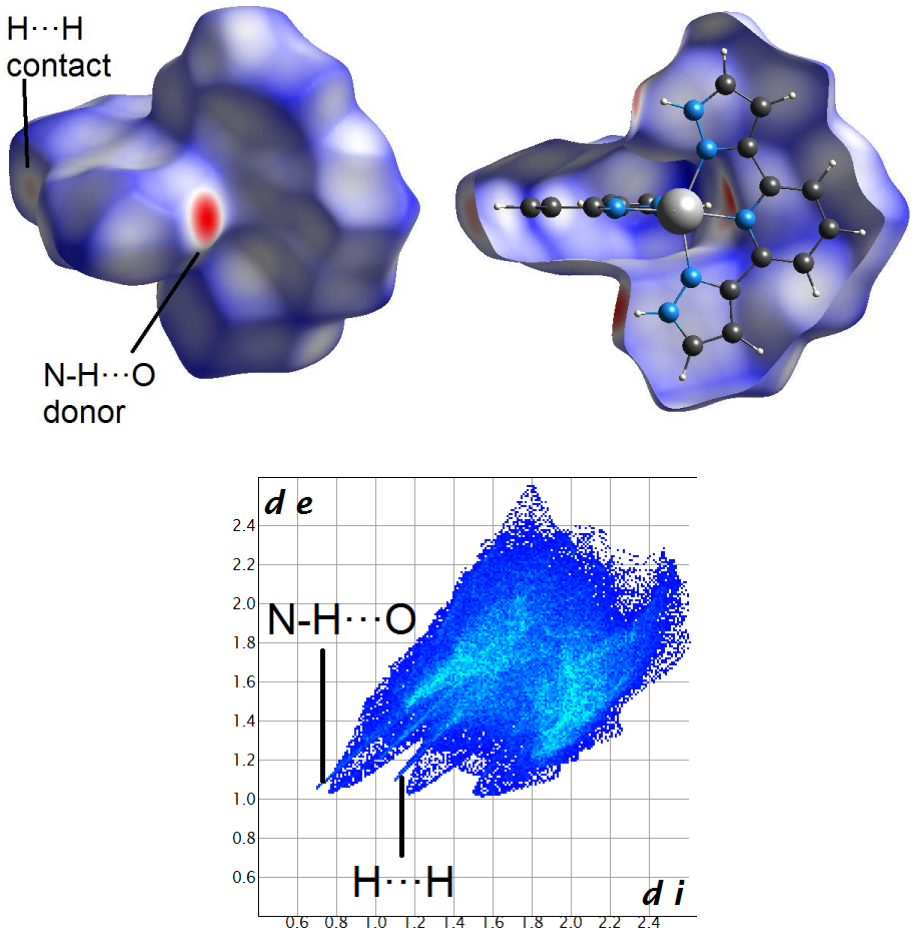

Figure 9.6: (top) Hirshfeld surface of the $[Fe(3\text{-bpp})_2]^{2+}$ cation from compound **i**, together a cut-away view of the complex within the surface. (bottom) 2D fingerprint plot derived from this surface.

The availability of the crystal structure of **1** in both the HS and LS states at the same temperature allows the comparison of the Hirshfeld surfaces independent of thermal effects (Figure 9.7). The surfaces of both spin states are remarkable for the far higher quantity of interactions visible on the surface when compared to **i**. There is the presence of hydrogen bonding motifs, both through the pyrazolyl rings and the phenol groups at the extremes of the H_4L ligand. There are, however, two new interactions when compared to the compound containing only the ligand 3-bpp. The terminal C-H groups of the aromatic ligands are seen to interact with the π-electron density of the pyrazolyl rings from neighbouring cations, as discussed in previous Chapters. This is seen as a slight red colouring to the participating C-H group, and as a pock-marking of the pyrazolyl acceptor. In the fingerprint plot, this is observed as a wing-type feature at (1.0, 1.6) and

(1.6, 1.0), although the latter is less clear because it is shrouded by points from other interactions. The other new interactions are the $\pi\cdots\pi$ stacking interactions concentrated at (1.8, 1.8), which are pivotal in the assembly of the terpyridine embrace. The change of spin state sees the merging of the long spikes that represent the hydrogen bonding within the lattice into one. Together with this, the wing-type feature of the C-H$\cdots\pi$ interaction becomes less well defined. The disappearance of many of the isolated spots around the O-H$\cdots$O and N-H$\cdots$O spikes is attributed to the disorder→order transition that accompanies the spin switch in compound **1**.

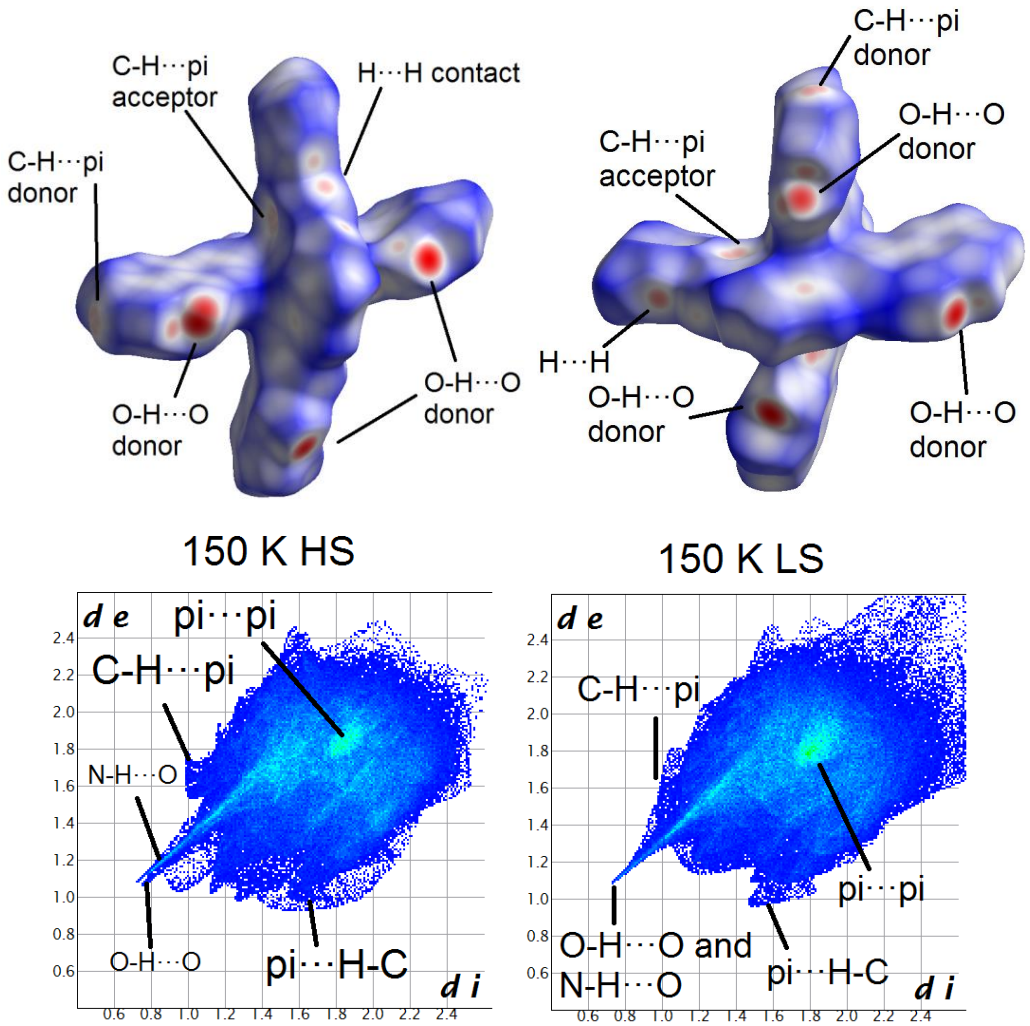

Figure 9.7: (left column) the Hirshfeld surface and corresponding fingerprint plot for the cation in **1** in the HS state and at the same temperature but in the LS state (right column).

This study could also be performed on the photo-induced HS state of **1**·PIHS, which was described in Chapter 5. The main conclusions drawn in that Chapter were that

1·PIHS was within a unit cell that resembled that of the LS state, and that the level of disorder in the anions and solvents was lower, again making **1**·PIHS resemble the LS state, albeit with HS cations. The fingerprint analysis of this photo-induced meta-stable state supports these conclusions (Figure 9.8). While there are features common to the HS fingerprint, such as the shape of the C-H···π wing, the main spike that represents the hydrogen bonding motifs is the same as that present in the LS fingerprint, and the lack of isolated points around these features attests to the lower disorder of **1**·PIHS when compared to the HS state of **1**. It was this discrepancy in the structural disorder that was used as the justification for applying a two-step model to the isothermal relaxation of the thermally trapped phase of compound **1**.

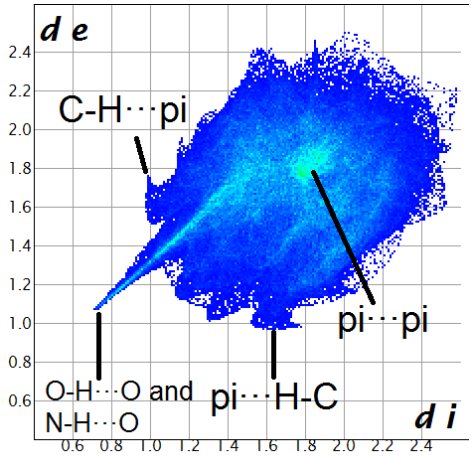

Figure 9.8: Fingerprint plot for the Hirshfeld surface of the cation in the photo-excited state of compound **1**.

The appeal of this technique to compare systems which show different magnetic behaviour in spite of apparently high structural similarity is therefore clear. This is particularly relevant in the case of compound **3**, which has the same composition as **1**, and apparently an array of intermolecular interactions which resembles that of **1**. The fingerprint plot derived from **3**'s Hirshfeld surface is displayed in Figure 9.9. The plot shares the π···π stacking interaction shown in **1** in the HS state, however, the spot is more diffuse around the region (1.8, 1.8), indicating a lower efficiency of packing associated with this contact. The differing degree of disorder with respect to **1** is the cause of the different appearance of the plots around the spikes that are due to the hydrogen bonding interactions. This is seen directly by the clean observation of the pi···H-C interaction which, in **1**, is beneath and surrounded by many other dots. The O-H···O hydrogen bonds

are seen to be less strongly directional, which results in a broader appearance of the feature in the plot, when compared to the two sharply defined spikes in Figure 9.7. It could be that all of these small, subtle differences, which are easily observed through this type of Hirshfeld analysis, are what lie behind the absence of SCO in compound **3**.

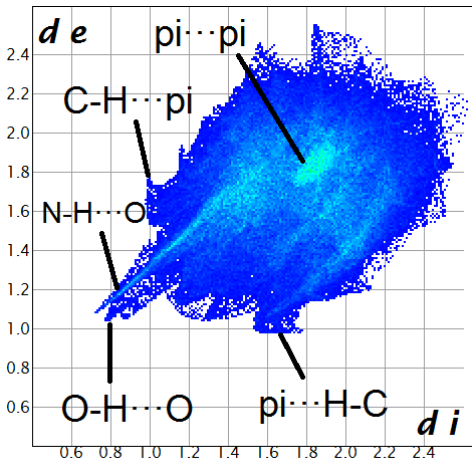

Figure 9.9 Fingerprint plot for the Hirshfeld surface of the cation in compound **3**.

The analysis of compound **5** showed that the Hirshfeld surface had little evidence of extensive intermolecular interactions (Figure 9.10). There are red patches on the surface which can be assigned to hydrogen bonding motifs, between the pyrazolyl or phenol rings and solvents or anions in the crystal, and this gives rise to one of the few strong features in the corresponding fingerprint plot. The surface also has significant blue regions, signifying that the distance between neighbouring atoms is large. This inefficient packing is represented in the fingerprint plot by the high number of contacts in regions beyond 2.2 along a given axis. There is a notable absence of the C-H···π interactions which reinforce the terpyridine embrace.[34, 35] The findings here are similar to those in Chapter 6. The action of spin-inactive entities in the lattice has a crucial effect on the crystal packing, which constitutes the basis of communication between the cations. The inefficient crystal packing, and the distortion it induces in the cation (see Sections 9.2 and 9.3) are therefore posited as the reason that **5** does not display SCO, with a similar effect seen in compound **4**.

Compound **7**, which displays a partial SCO with hysteresis, gives rise to the surface and fingerprint plot shown in Figure 9.11. The surface contains many features due to the

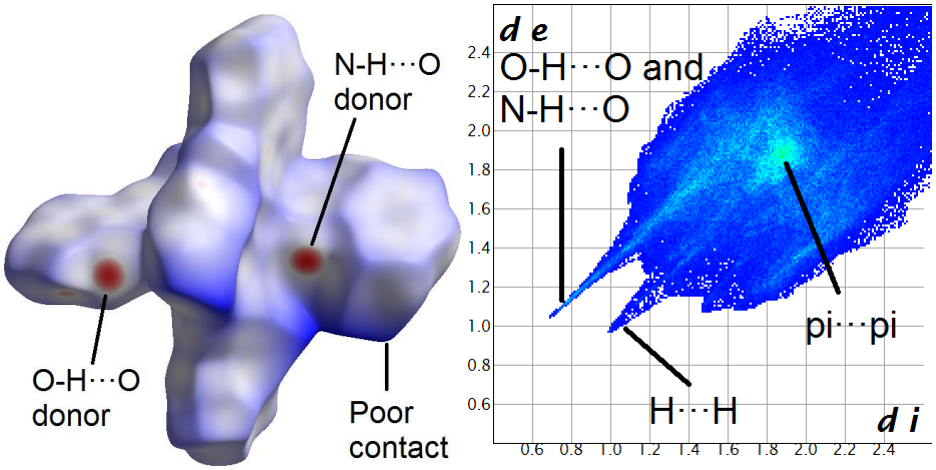

Figure 9.10 (left) The Hirshfeld surface and corresponding fingerprint plot (right) for the cation in compound **5**.

hydrogen bonding seen in the crystal structure, and also has the pock-marking in the centre of a pyrazolyl ring which is brought about by the C-H···π edge-to-face contacts in the lattice. These contacts are notable in their presence when contrasted with **5**, however they are not as well-defined as those observed in **1**. So, it would be clear from inspection of the Hirshfeld surfaces that, were they to give SCO, **7** would be more likely to show a cooperative transition than **5**.

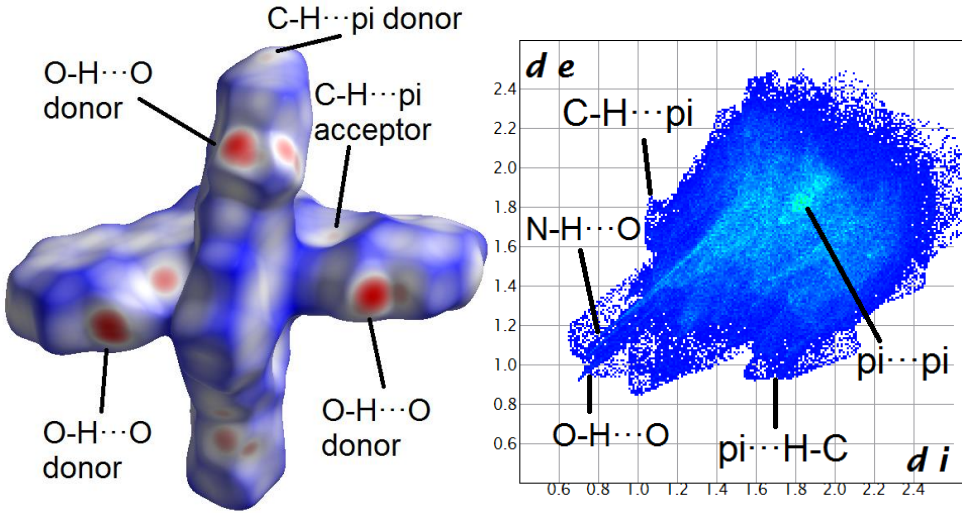

Figure 9.11 (left) The Hirshfeld surface and corresponding fingerprint plot (right) for the cation in compound **7**.

Compound **11**, which contains the H_2L1 ligand, gives rise to a Hirshfeld surface that has even fewer features than that yielded by **5** (Figure 9.12). There are extended regions

of inefficient packing, induced by the bulky methoxy group that is appended to the extremes of the ligand. This is reflected in the fingerprint plot by the huge number of points at the edge of the graph. This inefficient packing also impacts upon the cation's ability to participate in the face-to-face $\pi\cdots\pi$ stacking interactions that form the basis of the terpyridine embrace. There is a slight feature at (1.8, 1.8) in the fingerprint, but it does not possess the same intensity observed in the other compounds. While that particular interaction is nearly absent, there is still the presence of the edge-to-face C-H$\cdots\pi$ interactions, although the shape of the feature is distinct to that seen in the SCO compounds **1** and **7**. The large number of points in the fingerprint around (0.8, 0.8), which corresponds to a distance too short to realistically represent an intermolecular interaction, is due to the crystallographic disorder in the structure.

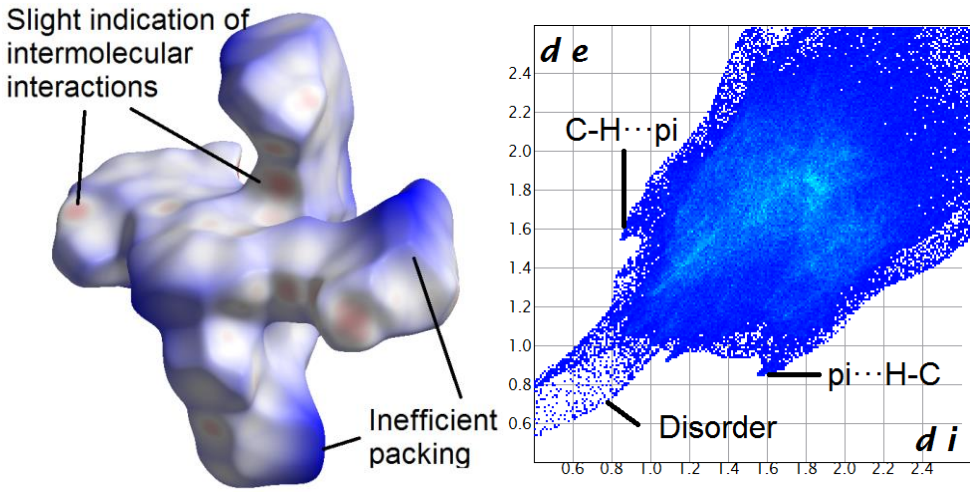

Figure 9.12 (left) The Hirshfeld surface and corresponding fingerprint plot (right) for the cation in compound **11**.

9.6 Concluding remarks

In this Chapter, which has compiled X-ray data for all of the mononuclear compounds presented in this thesis and compared them with the family of 3-bpp compounds that is available in the literature, the influence of both local and long-range structural characteristics has been used to rationalise the magnetic behaviour that was measured in the preceding Chapters. The local study involved looking solely at how the cations within these systems are distorted, whether as a consequence of the packing forces within the lattice, or as a result of Jahn-Teller distortion. Of the four distortion parameters studied, θ, the dihedral angle formed by the approximately perpendicular coordination of the two

ligands, was shown to have the least bearing on the magnetic properties. While the majority of LS systems showed values close to 90°, there are many examples of higher deviation from this value, spanning almost the same range as the HS systems. The *trans*-N-Fe-N angle was found to have a more important bearing. If this angle was below 170°, then an absence of SCO behaviour is registered, without exception. This finding is in line with the previous study by Halcrow and co-workers, who used DFT calculations to ascribe this absence to a loss of degeneracy in the e_g orbitals around highly distorted Fe(II) ions, which results in the "trapping" of the metal ion in the HS state, even on varying the temperature.[11] The parameters Σ and Θ were more clearly correlated with the spin state, displaying quite clear ranges of values for the quintet and singlet states. This trend was marked enough to be able to distinguish between systems that were fully in one state or another, and those that were to be found in a mixed spin state. The study of local geometries was then continued by applying Continuous Symmetry Measures. Here, as expected, the HS cations were found to further away in nature than the LS cations from an ideal octahedron. The proximity of all of the systems to the pathway associated with the Bailar twist was found to be limited, presumably due to the geometric constraints imposed by the tridentate ligands. It is clear from all of the studies that the HS electronic configuration allows for a greater distortion of coordination octahedron when compared to LS systems, with the final structure defined by the action of crystal packing effects.

The interactions that constitute these packing effects can be broken down into a 2D fingerprint plot through the method of Hirshfeld surface analysis, which was used to look at the intermolecular interactions. This technique confirmed many of the intermolecular interactions that were highlighted in the preceding Chapters. These interactions had been chosen through interpretation of the single crystal X-ray diffraction structures. While this approach allowed specific interactions to be measured and proposed as significant, the Hirshfeld surface analysis allows for a more overall picture of the crystal lattice and gives actual evidence of a feature such as inefficient crystal packing – something which may be intuited from inspection of the structure, but is confirmed by fingerprint plots. Because this analysis provides insights into long-range effects, it is useful for the rationalisation of magnetic properties in systems which superficially appear to be very, very similar.

9.7 References

1. M. A. Halcrow, *Chem. Soc. Rev.*, 2011, **40**, 4119-4142.
2. M. A. Halcrow, *Coord. Chem. Rev.*, 2009, **253**, 2493-2514.
3. P. Guionneau, M. Marchivie, G. Bravic, J.-F. Létard and D. Chasseau, *Top. Curr. Chem.*, 2004, **234**, 97-128.
4. H. Zabrodsky, S. Peleg and D. Avnir, *J. Am. Chem. Soc.*, 1992, **114**, 7843-7851.
5. S. Alvarez, *J. Am. Chem. Soc.*, 2003, **125**, 6795-6802.
6. J. J. McKinnon, A. S. Mitchell and M. A. Spackman, *Chem.-Eur. J.*, 1998, **4**, 2136-2141.
7. H. J. Shepherd, P. Rosa, L. Vendier, N. Casati, J.-F. Letard, A. Bousseksou, P. Guionneau and G. Molnar, *Phys. Chem. Chem. Phys.*, 2012, **14**, 5265-5271.
8. A. Grosjean, N. Daro, B. Kauffmann, A. Kaiba, J. F. Letard and P. Guionneau, *Chem. Commun.*, 2011, **47**, 12382-12384.
9. M. A. Spackman and J. J. McKinnon, *CrystEngComm*, 2002, 378-392.
10. V. A. Money, I. R. Evans, M. A. Halcrow, A. E. Goeta and J. A. K. Howard, *Chem. Commun.*, 2003, 158-159.
11. J. M. Holland, J. A. McAllister, C. A. Kilner, M. Thornton-Pett, A. J. Bridgeman and M. A. Halcrow, *J. Chem. Soc. Dalton Trans.*, 2002, 548-554.
12. J. Elhaik, D. J. Evans, C. A. Kilner and M. A. Halcrow, *Dalton Trans.*, 2005, 1693-1700.
13. J. K. McCusker, A. L. Rheingold and D. N. Hendrickson, *Inorg. Chem.*, 1996, **35**, 2100-2112.
14. M. G. B. Drew, C. J. Harding, V. McKee, G. G. Morgan and J. Nelson, *J. Chem. Soc., Chem. Commun.*, 1995, 1035-1038.
15. M. Marchivie, P. Guionneau, J. F. Letard and D. Chasseau, *Acta Cryst. B*, 2003, **59**, 479-486.
16. M. L. Scudder, D. C. Craig and H. A. Goodwin, *CrystEngComm*, 2005, **7**, 642-649.
17. E. Coronado, J. R. Galán Mascarós, M. C. Giménez-López, M. Almeida and J. C. Waerenborgh, *Polyhedron*, 2007, **26**, 1838-1844.
18. M. Clemente-León, E. Coronado, M. C. Giménez-López and F. M. Romero, *Inorg. Chem.*, 2007, **46**, 11266-11276.
19. E. Coronado, M. C. Giménez-López, C. Giménez-Saiz, J. M. Martínez-Agudo and F. M. Romero, *Polyhedron*, 2003, **22**, 2375-2380.
20. T. D. Roberts, F. Tuna, T. L. Malkin, C. A. Kilner and M. A. Halcrow, *Chem. Sci.*, 2012, **3**, 349-354.
21. M. C. Giménez-López, M. Clemente-León, E. Coronado, F. M. Romero, S. Shova and J.-P. Tuchagues, *Eur. J. Inorg. Chem.*, 2005, 2783-2787.
22. K. H. Sugiyarto, M. L. Scudder, D. C. Craig and H. A. Goodwin, *Aust. J. Chem.*, 2000, **53**, 755-765.
23. K. H. Sugiyarto, K. Weitzner, D. C. Craig and H. A. Goodwin, *Aust. J. Chem.*, 1997, **50**, 869-873.
24. S. A. Barrett, C. A. Kilner and M. A. Halcrow, *Dalton Trans.*, 2011, 12021-12024.
25. E. Coronado, M. Carmen Giménez-López, C. Giménez-Saiz and F. M. Romero, *CrystEngComm*, 2009, **11**, 2198-2203.
26. E. Coronado, J. C. Dias, M. C. Giménez-López, C. Giménez-Saiz and C. J. Gómez-Garcia, *J. Mol. Struct.*, 2008, **890**, 215-220.

27. K. H. Sugiyarto, W. A. McHale, D. C. Craig, A. D. Rae, M. L. Scudder and H. A. Goodwin, *Dalton Trans.*, 2003, 2443-2448.
28. K. H. Sugiyarto, D. C. Craig, A. D. Rae and H. A. Goodwin, *Aust. J. Chem.*, 1994, **47**, 869-890.
29. M. Clemente-León, E. Coronado, M. Carmen Giménez-López, F. M. Romero, S. Asthana, C. Desplanches and J.-F. Létard, *Dalton Trans.*, 2009, 8087-8095.
30. I. A. Gass, S. R. Batten, C. M. Forsyth, B. Moubaraki, C. J. Schneider and K. S. Murray, *Coord. Chem. Rev.*, 2011, **255**, 2058-2067.
31. S. Alvarez, D. Avnir, M. Llunell and M. Pinsky, *New J. Chem.*, 2002, **26**, 996-1009.
32. S. K. Wolff, D. J. Grimwood, J. J. McKinnon, M. J. Turner, D. Jayatilaka and M. A. Spackman, 2012, University of Western Australia.
33. J. J. McKinnon, D. Jayatilaka and M. A. Spackman, *Chem. Commun.*, 2007, 3814-3816.
34. J. McMurtrie and I. Dance, *CrystEngComm*, 2005, **7**, 216-229.
35. M. L. Scudder, H. A. Goodwin and I. G. Dance, *New J. Chem.*, 1999, **23**, 695-705.